

Generation of pure spin circular current in an open magnetic quantum ring with vanishing net magnetization

Debjani Das Gupta  and Santanu K. Maiti *

Physics and Applied Mathematics Unit, Indian Statistical Institute, 203 Barrackpore Trunk Road, Kolkata-700 108, India



(Received 8 March 2023; revised 13 October 2023; accepted 2 November 2023; published 21 November 2023)

We report the existence of a nondecaying circular spin current in an antiferromagnetic (AFM) quantum ring with zero net magnetization. In the presence of a finite voltage bias, a net circular spin current is generated in the ring geometry without accompanying any charge current. Such a bias-driven pure spin circular current in a magnetic ring with vanishing net magnetization has not been reported so far to the best of our knowledge. Employing a tight-binding framework to describe the nanojunction which is formed by connecting the AFM ring with two electrodes, we compute spin-dependent transport quantities along with spin circular current using the standard Green's function formalism. Most of the results are analyzed for the AFM ring where neighboring magnetic moments are arranged in antiparallel directions and different other configurations of magnetic moments are also taken into account for comparison. Various aspects are critically discussed like ring-electrode interface sensitivity, impurities at different lattice sites, ring-electrode coupling strength, spin-dependent scattering factor, Fermi energy, and system size, to make the present communication a self-contained one. For some input conditions, a nonzero circular charge current may appear but that is too small compared to the spin circular current. All the results are valid for a wide range of physical parameters which proves the robustness of the phenomenon of bias-driven circular spin current in an AFM nanoring. In the end, we also provide experimental perspectives for designing AFM ring systems. Our analysis red paves the way for obtaining a pure spin current in open quantum systems, offering opportunities to explore various simple and complex AFM loop substructures in the presence of external baths.

DOI: [10.1103/PhysRevB.108.195428](https://doi.org/10.1103/PhysRevB.108.195428)

I. INTRODUCTION

The phenomenon of nondecaying circular charge current in an isolated quantum ring (not attached to external electrodes) has been a well-known topic over many years [1–4]. Büttiker, Imry, and Landauer first proposed [1] that when a magnetic flux threads a conducting loop, commonly referred to as Aharonov-Bohm flux [5–7], a charge current is generated, and once this current is established it does not vanish even when the flux is removed. This is the so-called flux-driven persistent charge current in an isolated loop conductor. Following this proposition, later a substantial amount of theoretical [8–10] and experimental [11–14] works have been done considering different kinds of simple and complex loop conductors exploiting many fascinating results.

Analogous to persistent charge current, a persistent spin current is also obtained in an isolated quantum ring in presence of a spin-dependent scattering mechanism [15–17]. Several propositions have been put forward along this line. For instance, a ferromagnetic ring can generate a circular spin current where the spin-dependent scattering takes place due to the interaction of itinerant electrons with local magnetic sites. This scattering mechanism is very common and has been considered extensively in different contexts [18–22]. Later another prescription came to light, where the scattering occurs due to spin-orbit (SO) coupling. Usually, two types

of spin-orbit coupled systems are considered, one is called Rashba SO coupled systems [23], and the other is known as Dresselhaus SO coupled ones [24]. Among them, Rashba SO coupling becomes more promising since its strength can be monitored by means of external gate electrodes [25]. Though controlled spin transfer can be achieved, there are some unavoidable limitations in SO coupled systems. One of the key issues is that the SO coupling strength is too weak [26], and hence, large separation between up and down spin channels cannot be achieved. The large channel mismatch is one of the key prerequisites to have a favorable spin-dependent transport phenomena.

Most of the studies available in the literature related to the phenomenon of circular charge current have concentrated on isolated ring conductors [4–10]. Recently another mechanism has been proposed, where it is shown that a nondecaying charge current can also be established in a quantum ring when it is connected to external electrodes [27–33]. In this case, magnetic flux is no longer required and the current is generated due to a finite voltage bias across the contact electrodes. This phenomenon is referred to as bias-driven circular current in an open quantum ring system. A very limited amount of work is available so far, and further probing is definitely required to get more insights into this phenomenon [27–33]. The bias-driven circular current needs a complete description of currents in different branches of a quantum system, and from the branch currents, one can get important information about conducting behavior of different branches.

*santanu.maiti@isical.ac.in

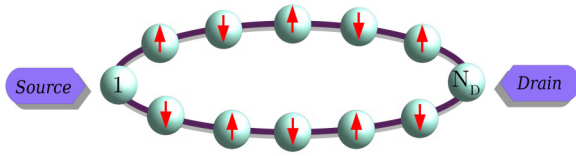


FIG. 1. Sketch of the ring nanojunction where an antiferromagnetic ring is symmetrically connected to source and drain electrodes. The neighboring magnetic moments are oriented in the opposite directions.

Like bias-driven persistent charge current, one can also think about persistent spin current in an open quantum system. The studies along this line are notably scarce. *The generation of bias-driven spin current in a nanoring, without accompanying any charge current is quite challenging, and in the present work, we essentially focus on this phenomenon.* Our motivations are many-fold. First, we want to investigate whether a magnetic ring system with zero net magnetization can generate a circular spin current in response to a voltage bias. Second, we want to explore, for such an antiferromagnetic system whether we can get spin current without accompanying any net charge current. Third, the sensitivity of circular spin current on different input parameters, i.e., we want to check the robustness of our analysis. These issues have not been discussed so far in the literature, to the best of our concern, and may open new insights into this phenomenon.

Antiferromagnetic systems are nowadays considered the promising functional elements for future generation spintronic devices due to their unique and diverse characteristic features over conventional ferromagnetic materials [34–39]. Among many, the most two important advantages are the existence of a higher temperature of phase transition of magnetic ordering [40,41] than the ferromagnetic samples, and, due to vanishing net magnetization the antiferromagnetic systems do not produce any stray fringe field [37,42]. These later systems are also very less perturbed due to the external magnetic field [36–38]. From the common wisdom, it seems that a magnetic quantum ring with zero net magnetization cannot produce any net spin circular current, as up and down spin energy channels are identical to each other. However, here we prove that it is absolutely possible, and the degree of current can be reasonably large. The other important finding of our work is that we can produce spin current without accompanying any charge circular current. We choose a tight-binding (TB) antiferromagnetic ring where the neighboring magnetic moments are oriented in opposite directions, which is the most common arrangement. The ring is sandwiched between two nonmagnetic contact electrodes (see Fig. 1). In the presence of symmetric ring-electrode junction configuration, interestingly we find that a reasonably large pure spin current is generated in the ring. To find the robustness of our analysis, we choose some other possible arrangements of local magnetic moments, setting the condition of vanishing net magnetization, and also analyze the behavior of circular spin current under different input conditions by changing the physical parameters in a wide range. In a few cases, circular charge current appears in the ring but its magnitude is too small compared to the

spin circular current. Notably, our results are highly robust as they are almost unperturbed in realistic conditions like in presence of impurities, orientations of magnetic moments, ring-electrode junction configurations, etc. All the relevant spin-dependent quantities are worked out based on the well-known Green’s function formalism [43–46]. In the end, we briefly discuss the experimental possibilities for designing AFM ring geometries that are considered in our work, for the sake of completeness.

The organization of the rest other parts is as follows. Section II deals with the description of one particular type of nanojunction where neighboring magnetic moments in the AFM ring are oriented in opposite directions, and, the theoretical framework for the calculations. All the numerical results of this AFM ring are presented and thoroughly scrutinized in Sec. III. Moreover, two other AFM rings with different arrangements of magnetic moments are taken into account and their results are also analyzed in Sec. III. In Sec. IV, we add a brief discussion about experimental possibilities for designing AFM rings. Finally, Sec. V, includes the summary of the present investigation.

II. PHYSICAL SYSTEM AND THEORETICAL FRAMEWORK

This section is divided into two parts. In one part (part A), we discuss the AFM ring nanojunction and tight-binding Hamiltonian for the nanojunction. In the other part (part B), the theoretical prescription is given for the calculation of different spin-dependent quantities.

A. AFM ring nanojunction and TB Hamiltonian

The nanojunction is formed by sandwiching an AFM ring between two contact electrodes. In our analysis, we consider three different kinds of AFM rings, based on the specific arrangement of local magnetic moments in the ring, for a comparative analysis. The junction with one such arrangement is schematically shown in Fig. 1 (other two will be discussed in the appropriate parts). The AFM ring, possessing N sites (N is taken to be even), is clamped between two nonmagnetic electrodes, those are labeled as source (S) and drain (D). The red arrows at different lattice sites represent the magnetic moments. In the ring of Fig. 1, we assume that the successive magnetic moments are aligned along $\pm Z$ directions. This is the most common antiferromagnetic configuration and we refer to this ring as ‘ring-1’. Instead of considering such a specific arrangement, as already mentioned, other possible configurations can also be taken into account, following the condition of vanishing net magnetization. The general orientation of any local magnetic moment at site i can be described using polar angle θ_i and azimuthal angle ϕ_i . The source electrode is always connected to site 1 of the ring, while the position of N_D where the drain is coupled can vary. Both the sites 1 and N_D are assumed to be nonmagnetic.

The spin-dependent scattering occurs due to the interaction of conduction electrons with local magnetic sites via the usual spin-moment interaction. It is relevant to note that, this scattering strength is reasonably large [26] compared to the other spin-dependent scatterings like spin-orbit coupling, Zeeman

splitting, etc., and this is one of the fundamental reasons of considering magnetic systems.

We employ a TB framework to illustrate the nanojunction. The Hamiltonian of the full system (viz, AFM ring with side-attached electrodes) is written as

$$H = H^R + H^{\text{elec}} + H^{\text{coup}}, \quad (1)$$

where different sub-Hamiltonians in the right side of Eq. (1) are associated with different parts of the nanojunction, and their forms are as follows. For the AFM ring, the Hamiltonian H^R reads as

$$H^R = \sum_i [c_i^\dagger (\epsilon_i - \vec{h}_i \cdot \vec{\sigma}) c_i + (c_i^\dagger t c_{i+1} + c_{i+1}^\dagger t c_i)], \quad (2)$$

where $c_i^\dagger = (c_{i\uparrow}^\dagger \ c_{i\downarrow}^\dagger)$. $c_{i\sigma}^\dagger$, $c_{i\sigma}$ are the fermionic operators with $\sigma = \uparrow, \downarrow$. ϵ_i and t are the site energy and hopping matrices respectively, and, they are $\epsilon_i = \text{diag}(\epsilon_{i\uparrow}, \epsilon_{i\downarrow})$ and $t = \text{diag}(t, t)$. $\epsilon_{i\sigma}$ is the site energy of an electron at i th site in the absence of any kind of magnetic scattering and t is the nearest-neighbor hopping (NNH) strength. \vec{h}_i is spin-dependent scattering factor which is the product of the spin-moment coupling strength J and the average local spin $\langle \vec{s}_i \rangle$. σ is the Pauli spin vector. In our formulation, σ_z is diagonal.

The sub-Hamiltonians H^{elec} and H^{coup} are associated with the contact electrodes and the coupling of the AFM ring with the electrodes. We assume that the electrodes are nonmagnetic in nature, and they are semi-infinite, one-dimensional, and reflectionless. It is no longer required to write the explicit forms of H^{elec} and H^{coup} as they can be understood quite easily (just like 1D TB chain). The electrodes are parameterized by the site energy ϵ_0 (same for both up and down spin electrons) and the NNH strength t_0 . The sites 1 and N_D of the AFM ring are coupled to S and D via the coupling parameters τ_S and τ_D , respectively.

B. Theoretical framework

To evaluate bias-driven circular current, be it charge or spin, we need to calculate the currents in individual bonds of the ring system, and we do that using the well-known Green's function formalism. First, we need to define a correlated Green's function which is [44,45,47]

$$G^n = G^R (f_S \Gamma_S + f_D \Gamma_D) G^A. \quad (3)$$

Here, Γ_S and Γ_D are the coupling matrices, and f_S , f_D are the Fermi functions of S and D, respectively. G^R and G^A are the retarded and advanced Green's functions, respectively, and they are [44,47]

$$G^R = (G^A)^\dagger = (E - H^R - \Sigma_S - \Sigma_D)^{-1} \quad (4)$$

where $\Sigma_{S(D)}$ is the self-energy due to S(D). The self-energy terms contain all the information of the electrodes. In presence of a finite bias V among these electrodes, their electrochemical potentials get changed and they are $\mu_S = E_F + eV/2$ and $\mu_D = E_F - eV/2$, where E_F is the equilibrium Fermi energy, and e is the electronic charge.

Using the correlated Green's function, bond current densities (current per unit energy) are evaluated. For an electron

with spin σ' which is transferred from site i to site j as spin σ , the bond current density is defined as [8,48,49]

$$J_{i\sigma' \rightarrow j\sigma} = \frac{2e}{h} \Im [H_{i\sigma',j\sigma}^R G_{j\sigma,i\sigma'}^n]. \quad (5)$$

The total bond current density is obtained by summing over incident spin and it becomes

$$J_{i \rightarrow j}^\sigma = \sum_{\sigma'} J_{i\sigma' \rightarrow j\sigma}. \quad (6)$$

Adding the contributions of all individual bonds, we get the circular current density which is expressed as

$$J_{\text{cir}}^\sigma = \sum_{\langle i,j \rangle} J_{i \rightarrow j}^\sigma. \quad (7)$$

To understand the behavior of J_{cir}^σ in a more simpler way, we can write it as a sum $J_{\text{cir}}^\sigma = J_U^\sigma + J_L^\sigma$, where J_U^σ and J_L^σ correspond to the bond current densities associated to the ‘‘upper’’ and ‘‘lower’’ arms of the ring nanojunction, respectively. We take positive sign of current when it flows in clockwise direction and the sign becomes negative when the current flows in opposite direction.

Now, we separately define the charge and spin current densities through the expressions [22]

$$J_{\text{cir}}^C = \frac{1}{N} (J_{\text{cir}}^\uparrow + J_{\text{cir}}^\downarrow); \quad J_{\text{cir}}^S = \frac{1}{N} (J_{\text{cir}}^\uparrow - J_{\text{cir}}^\downarrow). \quad (8)$$

Finally, to have charge and spin circular currents in the ring we need to integrate the respective current densities. They are [8,22,48]

$$I_{\text{cir}}^{C(S)} = \int J_{\text{cir}}^{C(S)} (f_S - f_D) dE. \quad (9)$$

As the sign of the individual current components can be both positive and negative, from the above definitions, it is expected that charge current might be zero while spin current is finite, and that is precisely our ultimate aim.

III. NUMERICAL RESULTS AND DISCUSSION

In what follows, we present and discuss our results. Three separate sub-sections are used for three distinct arrangements of magnetic moments associated with the AFM ring. Most of the results are associated with the nanojunction of ring-1 type (placed in Sec. A), and for the other two configurations the essential results are placed in Secs. B and C, for a direct comparison. All the energies are measured in units of electron-volt (eV). Throughout the numerical calculations we choose $\epsilon_0 = 0$ and $t_0 = 2$ (TB parameters of the side-attached electrodes). The NNH strength t in the AFM ring is fixed at 1. In the absence of any disorder in the ring we choose $\epsilon_{i\uparrow} = \epsilon_{i\downarrow} = 0$, while for the disordered case these energies are chosen randomly (more clearly described in the subsequent subsection). Unless specified, the other physical parameters are: $h_i = 1$, $\tau_S = \tau_D = 1$, $N = 32$, and the results are worked out for symmetric ring-electrode junction configuration considering perfect ring and fixing the system temperature at 100 K. For the sake of completeness of our investigation, the characteristics features of circular spin currents under different input conditions viz, by changing the spin-dependent

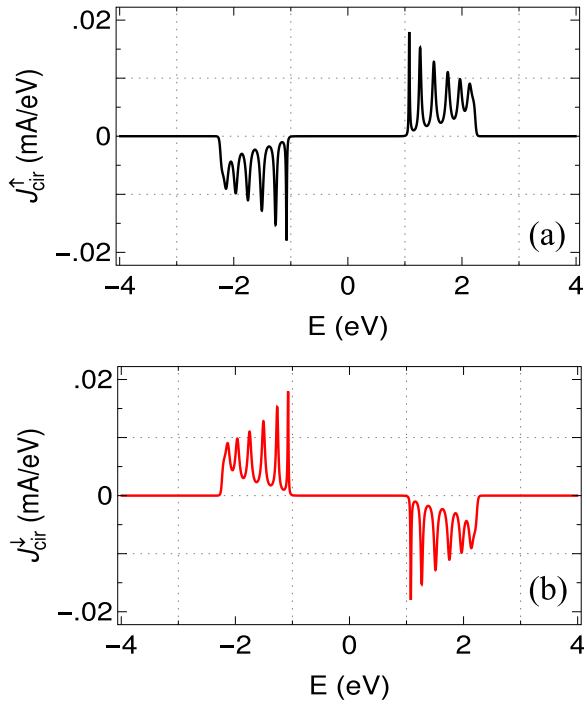


FIG. 2. Variation of (a) up and (b) down spin circular current densities as a function of energy. Here we choose the ring size $N = 32$, Fermi energy $E_F = 0$ and the bias voltage $V = 6$ V.

scattering parameter (h_i), ring-electrode coupling (τ_S, τ_D), ring size (N), disorder, ring-electrode interface configurations, etc., are also discussed one by one in the appropriate parts.

A. Nanojunction where neighboring magnetic moments in the AFM ring are aligned along $\pm Z$ directions

This section contains the results of the ring nanojunction where the neighboring magnetic moments in the AFM ring are oriented along

$\pm Z$ directions. As the net current density and the corresponding current specifically depend on the current densities of the individual components associated with up and down spin electrons, let us start with Fig. 2 where the variation of up and down spin current densities are shown. The results are computed for the symmetric ring-electrode interface configuration setting $E_F = 0$. Several interesting features are obtained those are as follows. Both up and down spin current densities exhibit some peaks and dips with different heights at some particular energies, while for other energies no such peaks or dips appear. These peaks and dips are associated with the discrete energy channels of the AFM ring which is sandwiched between the source and drain electrodes, and depending on the nature of the resonant energy channels we get higher or lower current densities. Unlike transport current density, i.e., current density in the contact electrodes, the circular current density can be positive as well as negative. Two different signs indicate the propagation of electrons in two different directions (clockwise and counterclockwise). This is expected as the central region is a ring system which provides two possible paths to flow electrons from source to the drain. Carefully inspecting the current density profiles

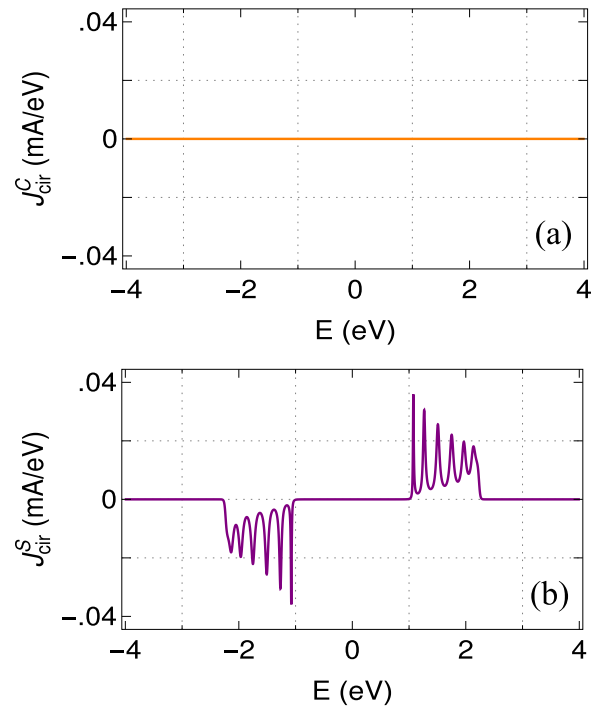


FIG. 3. Charge and spin circular current densities, shown in (a) and (b) respectively, as a function of energy. All the physical parameters remain same as used in Fig. 2.

of up and down spin electrons it is seen that in each case the spectrum is anti-symmetric around $E = 0$. At the same time, the other key feature is that the spin dependent current densities are exactly opposite to each other. It means, for a particular energy if up spin current density provides a peak or dip, the down spin current density is exactly opposite to that. The completely opposite natures (magnitude and sign) of $J_{\text{cir}}^{\uparrow}$ and $J_{\text{cir}}^{\downarrow}$ (Fig. 2) arise due to the consideration of the identical number of magnetic moments that are aligned in opposite directions in the upper and lower arms of the ring, and the ring is coupled to the electrodes symmetrically (arm lengths are equal).

From the profiles of spin specific circular current densities, presented in Fig. 2, the characteristic features of charge and spin circular current densities can easily be followed. The results are shown in Fig. 3, for the identical junction setup as used in Fig. 2. The charge current density drops exactly to zero for the entire energy window [Fig. 3(a)], as $J_{\text{cir}}^{\uparrow}$ and $J_{\text{cir}}^{\downarrow}$ are exactly opposite to each other. On the other hand, the spin current density becomes finite and in this case it is two times the individual spin component [Fig. 3(b)]. Thus a finite spin current density can be generated without having any charge current density. Here it is relevant to note that, such a situation cannot be established if the ring is a ferromagnetic one, where all the moments are oriented in one particular direction. Though spin current density is finite for some energy regions, the choice of $E_F = 0$ leads to exactly identical peaks and dips around it. Therefore, for this typical E_F , we cannot get any net spin current as it is obtained by integrating the current density function following Eq. (9). With increasing the energy window, equal number of peaks and dips appear

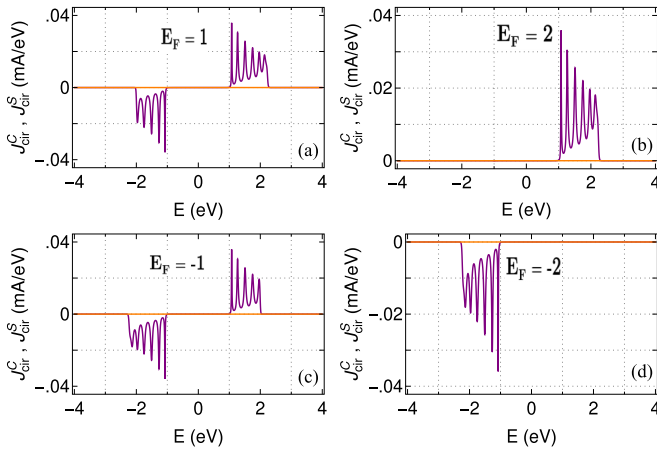


FIG. 4. Spin (indigo color) and charge (orange color) circular current densities as a function of energy E in four distinct Fermi energies, to explore the specific role of Fermi energy. The ring size and the ring-electrode junction configuration are same as used in Fig. 2.

within the window resulting a vanishing net current. It clearly manifests that the choice of E_F is undoubtedly important, and this is common [50–54] to observe any other spin-dependent phenomena like spin polarization, spin current rectification and to name a few.

To have a finite spin circular current we need to choose E_F in such a way that within the energy window for which the integration is made, the peaks and dips are nonuniform. Otherwise, the current will be zero due to mutual cancellation. In Fig. 4, we select four such typical Fermi energies around which the spin current density profile is nonuniform. The charge current density becomes always zero (orange line), as expected. Several other Fermi energies can also be chosen for which one can have the similar scenario. The effect of E_F directly enters into the correlated Green's function via the relation defined in Eq. (3). Using the density profiles given in Fig. 4, we compute spin circular current as a function of bias voltage and the results are shown in Fig. 5. Four different

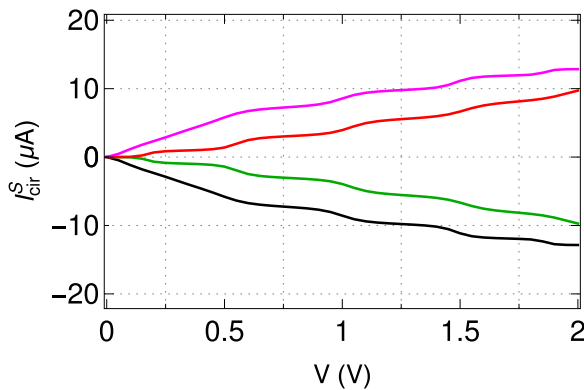


FIG. 5. Spin circular current as a function of bias voltage, at four distinct values of E_F , where the black, green, red and purple curves are associated with $E_F = -2, -1, 1,$ and 2 , respectively. The ring size and the ring-electrode junction configuration are same as used in Fig. 2.

colored curves are used for four distinct Fermi energies. In each case, the current provides quite a steplike behavior associated with the discrete peaks and dips of the density profile. The magnitude of the current is also reasonably large, that is indeed an interesting finding. Depending on the choice of E_F we can have positive or negative spin circular current in the ring.

Detailed physical argument for the generation of spin current. For a more complete description, here we elucidate the underlying mechanism responsible for the generation of circular spin current in a loop nanojunction. First, we concentrate on the bias driven charge circular current, and thus, ignore the spin degrees of freedom. If I_U and I_L are the currents in the upper and lower arms of a ring conductor which is clamped between S and D, then the circular charge current is defined by the average of these two currents viz, $(I_U + I_L)/N$, and the transport current (say, I_{tr}), i.e., current in the drain end is defined as $I_{tr} = (I_U - I_L)/N$ (a comprehensive description is given in Ref. [29]). For a symmetric ring nanojunction $I_U = -I_L$, and hence, the charge current completely vanishes. For this configuration, the identical magnitudes of the currents in the two arms are naturally expected, and the appearance of opposite sign is also easy to understand, otherwise the transport current will vanish [29]. Thus symmetric configuration is the primary requirement to have zero circular charge current. Now, consider the magnetic ring where spin degrees of freedom are involved. For our chosen AFM ring system, we find that $J_U^\uparrow = -J_L^\downarrow$ and $J_L^\uparrow = -J_U^\downarrow$, and these are directly associated to the arrangements of local magnetic moments in the two arms of the AFM ring. Therefore we reach to the relation $J_{cir}^\uparrow = -J_{cir}^\downarrow$. Since the up and down spin circular current densities have equal magnitudes and opposite signs, the definitions given in Eq. (8) lead to the complete disappearance of charge current density and the emergence of a finite spin current density. Integrating the spin current density [see Eq. (9)], we get the spin circular current associated with a finite bias voltage. For a particular junction configuration, the sign of the spin current essentially depends on the choice of the Fermi energy. If the spin current density exhibits peaks around the Fermi energy, it results in a positive spin current, while a negative spin current occurs when the density profile displays dips across the Fermi energy. When both peaks and dips are concerned, the sign depends on the dominating ones among them. A discussion about the role of Fermi energy on spin circular current is already given above. Some other factor are also involved that are explicitly addressed in the subsequent sections.

Following the above overall analysis of current densities and circular currents, now we critically explore the role of different input parameters on circular current in the AFM ring-1 system, and check how the results are robust.

1. Ring-electrode junction configuration: interface sensitivity

Quantum interference among the electronic waves passing through upper and lower arms of the ring plays an important role on circular current, and thus, it is indeed required to inspect the behavior of bias-driven circular current for different ring-electrode junction configurations. For a perfect AFM ring, once we break the symmetry among the two arms by

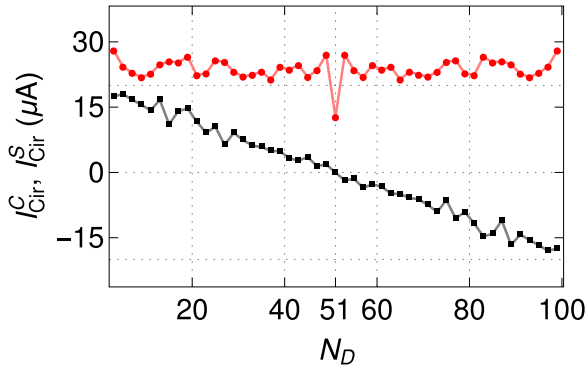


FIG. 6. Interface sensitivity on circular current. The spin (red curve) and charge (black curve) circular currents as a function of drain position N_D . The source is always connected to site 1 of the ring, as before. Here we set $N = 100$, $E_F = 1$ eV, and $V = 4$ V.

connecting the drain electrode asymmetrically, a net charge circular current appears along with the spin one. For an asymmetric ring-electrode junction configuration, the individual spin current components are no longer identical to each other, resulting in a nonzero charge current. The results are given in Fig. 6 for a 100-site AFM ring, where both charge (black color) and spin (red color) circular currents are shown at a particular bias voltage when the drain position is varied from site 3 to 100. One important observation is that, though charge current is finite for all the asymmetric junction configurations, it is always smaller than the spin current, and especially for the approximate range $40 \leq N_D \leq 60$, $I_{\text{cir}}^C \ll I_{\text{cir}}^S$. Due to quantum interference as we approach the symmetric junction configuration more closely, the charge current decreases, and eventually drops to zero for the symmetric junction setup ($N_D = 51$ for the 100-site ring). The other notable fact is that, the spin circular current is very less fluctuating for all the possible choices of drain connection (red curve of Fig. 6). So one can safely have circular spin current for any N_D , but to set vanishingly small charge current we need to choose N_D appropriately as clearly reflected from Fig. 6.

2. Effect of disorder

To inspect how disorder can perturb circular spin current and at the same time to check whether a large charge current appears or not, in this section, we discuss the role of disorder [55–59] on these quantities.

The disorder in the antiferromagnetic ring is included by choosing the site energies $\epsilon_{i\uparrow}$ and $\epsilon_{i\downarrow}$ randomly from a “Box” distribution function of width W . We always set the condition $\epsilon_{i\uparrow} = \epsilon_{i\downarrow}$. For $W = 0$, the ring becomes a perfect one. Figure 7 displays the variation of spin and charge circular currents as a function of bias voltage V at some distinct values of W . The result for $W = 0$ (green curve) is also superimposed in each spectrum for a better comparison. Here we set $N = 32$, $E_F = 1$ eV, and compute all the curves, for the disordered ring, taking the average over 50 distinct random configurations. In the absence of W , charge current completely vanishes [green line of Fig. 7(b)], as expected, since the ring is connected symmetrically with the contact electrodes. Under this condition, the spin current becomes a maximum [green curve

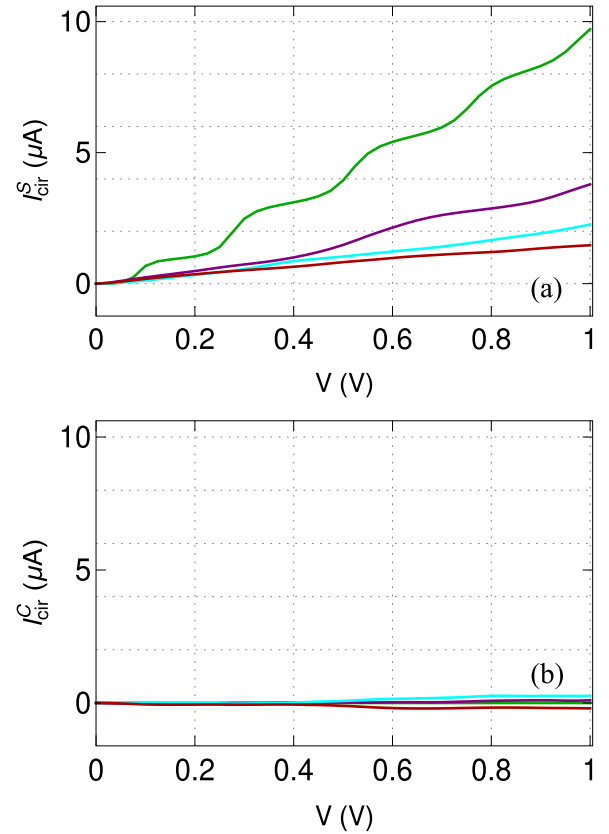


FIG. 7. Role of disorder W . The spin and charge circular currents, shown in (a) and (b) respectively, as a function of bias voltage at some typical disorder strengths for symmetrically connected ring nanojunction with $E_F = 1$ eV and $N = 32$. In each spectrum, the green, magenta, cyan and maroon colored curves are for $W = 0, 0.5, 1$, and 1.5 , respectively. The results are obtained by averaging over 50 distinct random disordered configurations.

of Fig. 7(a)]. When the disorder is introduced, along with spin current, a finite charge current also appears due to the breaking of the symmetry among the upper and lower arms, but the notable fact is that the charge current is almost vanishingly small than the circular spin current for the entire bias window. Moreover, the spin current is quite appreciable even when the disorder is too large. This is undoubtedly quite interesting.

3. Role of electrode-ring coupling

In this sub-section we discuss the specific role of ring-electrode coupling strength (τ_S, τ_D), which controls the flow of particles from the electrode to the ring system. This coupling can be easily tuned in suitable experimental setup by changing the distance of separation between the ring and the electrodes. In Fig. 8, we show the results for two distinct coupling strengths, 0.5 and 0.8, those are respectively presented in (a) and (b), respectively. The charge circular current is zero throughout the bias window (black line) as we set symmetric ring-electrode junction configuration. The spin circular current, on the other hand, provides reasonably large values. In Fig. 5, I_{cir}^S - V curve for $E_F = 2$ is shown (purple curve) when $\tau_S = \tau_D = 1$ eV, and in Fig. 8, I_{cir}^S - V curves are plotted for the same E_F at two other coupling strengths. Comparing

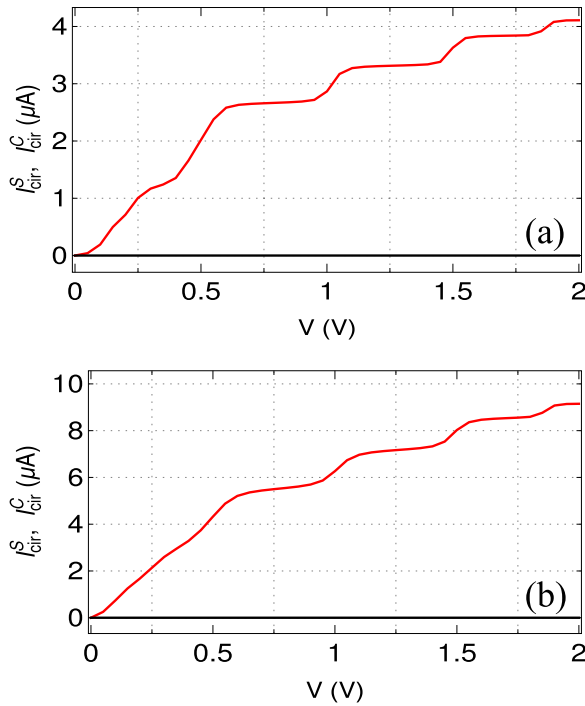


FIG. 8. Effect of ring-electrode coupling. Circular spin (red color) and charge (black color) currents as a function of bias voltage for two different ring-electrode coupling strengths, where (a) $\tau_S = \tau_D = 0.5$ and (b) $\tau_S = \tau_D = 0.8$. Here we set $E_F = 2$ eV. The ring size and the ring-electrode junction configuration are same as used in Fig. 2.

all these results, it is seen that the spin current decreases with $\tau_{S(D)}$, but in all these cases the current magnitude is appreciable. This slight reduction of current with lowering the ring-electrode coupling can nicely be explained as follows. As already mentioned, circular current is obtained by integrating the current density function, multiplied by the difference of f_S and f_D [see Eq. (9)]. In the current density profile, we get peaks and dips, which are quite analogous to the resonant transmission peaks in a nanojunction [60–62] (dips cannot be observed in the transmission spectrum as the probability is always positive, but for the circular current both peaks and dips are available due to clockwise and anticlockwise movements of particles). The widths of the peaks and dips depend on the ring-electrode coupling. For weak coupling, the widths are narrow, while they get broadened in the strong-coupling limit. Therefore, while integrating the density profile, we get lesser and higher currents for the weak and strong coupling limits respectively. It gives an interesting message that the magnitude of spin circular current can be tuned selectively by adjusting the coupling parameter. Here it is relevant to point out that, such coupling effect on transmission probability and junction current (or we can say drain current) has already been reported in the literature in different other contemporary articles [60–62].

4. Effect of spin dependent scattering factor

The spin dependent scattering factor h (in our calculation we choose $h_i = h$ for all i) is no doubt one of the primary

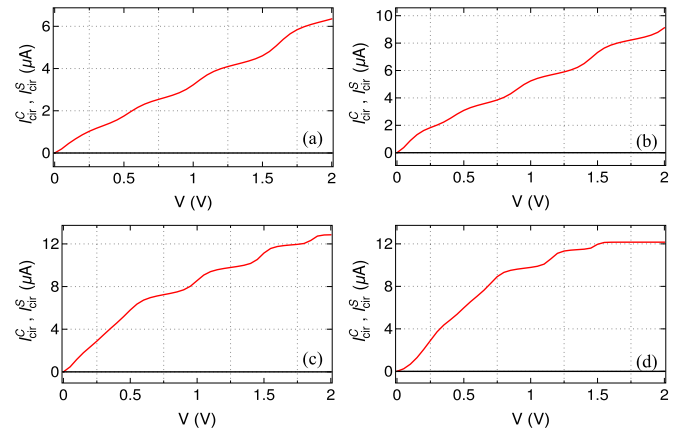


FIG. 9. Role of spin-dependent scattering parameter. Spin (red) and charge (black) circular currents as a function of bias voltage for four different values of the spin-dependent scattering parameter h (in our calculation, h_i 's are same and hence we can safely skip the index i). In (a)–(d), we choose $h = 0.4, 0.6, 1, 1.2$ respectively. The results are worked out for the same ring size and junction configuration as mentioned in Fig. 2. Here the Fermi energy is fixed at 2 eV.

parameters that is involved to have the spin specific phenomenon, and thus, its dependence needs to be checked. The higher value of h leads to a large mismatch among the up and down spin energy channels, and hence more favorable response might be expected. In Fig. 9, we display the variation of charge and spin circular currents as a function of bias voltage for four distinct values of the spin-dependent scattering parameter h those are given in (a) to (d). The results are worked out for the symmetric ring-electrode junction configuration. The charge current (black line) is always zero in each case, as expected. For the spin current (red curve), quite a considerable change in current magnitude is seen. Most importantly, we find that for large h , the spin current is reasonably large even at low biases. Achieving of higher spin circular current at lower bias is one of the key requirements of our study, and here it is successfully established.

5. How spin current is perturbed with slight variation of N_D from symmetric configuration?

It is already established from the above discussion that for the symmetric ring-electrode junction configuration, we get pure spin circular current as the charge circular current becomes exactly zero. Now the question is how the spin current is perturbed if we just break the symmetric junction configuration by slightly shifting the drain position, i.e., by making a minor difference between the two arm lengths. This inspection is no doubt required to check the robustness of our analysis. To reveal this fact in Fig. 10, we consider two different junction configurations where the drain position is slightly shifted from the symmetric configuration. The symmetric case is also included, for the comparative analysis. Like earlier, the source electrode is always coupled to site 1 of the AFM ring. For the symmetric configuration N_D becomes identical to $(N/2 + 1)$ [schematic setup is given in Fig. 10(a)]. For the other two configurations, we choose $N_D = (N/2 - 1)$ and $N_D = (N/2 + 3)$, and they are schematically shown in

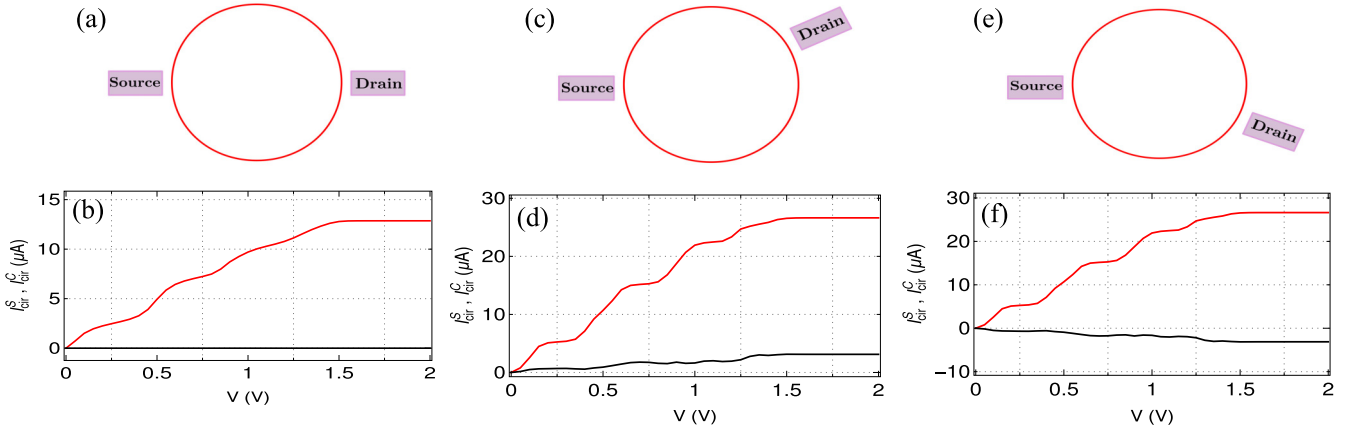


FIG. 10. These results explore how the spin current is sensitive if the drain electrode is slightly shifted from the symmetric junction configuration. The source is coupled to site 1 of the ring. For the symmetric configuration $N_D = (N/2 + 1)$ [schematically shown in (a)], and the results of charge and spin circular currents are shown in (b). In (c) and (e), we choose $N_D = (N/2 - 1)$ and $N_D = (N/2 + 3)$, respectively, and for these configurations the results are given in (d) and (f), respectively. All these results are found for a 32-site ring considering $E_F = 1.5$ eV. The red and black curves are for the spin and charge circular currents, respectively.

Figs. 10(c) and 10(e), respectively. The results for the three different junction configurations are given in the second row of Fig. 10, where the red and black curves are for the circular spin and charge currents, respectively. The outcomes are interesting and significant as well. For both the asymmetric configurations, a nonzero charge current appears, but the fact is that this current is too small almost for the entire bias window [black curves of Figs. 10(d) and 10(f)], compared to the spin counterparts [red curves of Figs. 10(d) and 10(f)]. The other notable thing is that, for these asymmetric junction setups, the spin circular currents are too large and more than two times higher than the symmetric junction. All these features are directly associated to the quantum interference of electronic waves passing through upper and lower arms of the ring nanojunction. Here we want to reiterate one point that in Fig. 6 the dependence of spin circular current, at a particular bias voltage, on N_D is already shown by varying N_D in a wide range. The spin current exhibits a very less fluctuation with N_D . Thus it can be emphasized that the studied spin circular current is quite robust, even when the drain position gets shifted. But, as charge circular current may appear for any arbitrary drain position, we need to select it accordingly such that the charge current becomes negligibly small.

6. Dependence of spin circular current on ring size

To inspect whether ring size has any significant effect on spin circular current, in Fig. 11, we present the variation of I_{cir}^S with N , by changing N in a broad range. Here we always set the symmetric ring-electrode junction configuration. For lower values of N , the current sharply decreases with N , but after a few ring sizes the current becomes almost constant. Very little fluctuation is obtained in current with the ring size, and this phenomenon still continues for much higher values of N (not shown here), which we confirm through our detailed numerical calculations. The almost constant magnitude of circular spin current can be explained as follows. The circular current is obtained by taking the contributions of individual bonds of the ring. Adding the contributions of all the bonds,

we divide by the factor N [see Eqs. (7) and (8)] to get the circular current. With increasing N , the number of bonds gets increased and thus the total current. Finally, when we divide the sum by N , the ratio becomes almost constant. This is an interesting phenomenon, unlike the transport current which usually gets reduced by enhancing the system size. This result gives a clear indication that we can observe the phenomenon of bias-driven spin circular current even when the ring size is too large, that is quite interesting from the experimental view point.

7. Simultaneous variation of spin circular current with Fermi energy and bias voltage

The above discussed results are worked out at some typical Fermi energies, and it is already explained that the choice of Fermi energy is quite crucial such that the peaks and dips of current density profile do not mutually cancel to each other. Now the question is how sensitive the choice of Fermi energy is. To answer it, in Fig. 12, we present a density plot where the simultaneous variation of circular spin current as functions of bias voltage and Fermi energy is given. Both the

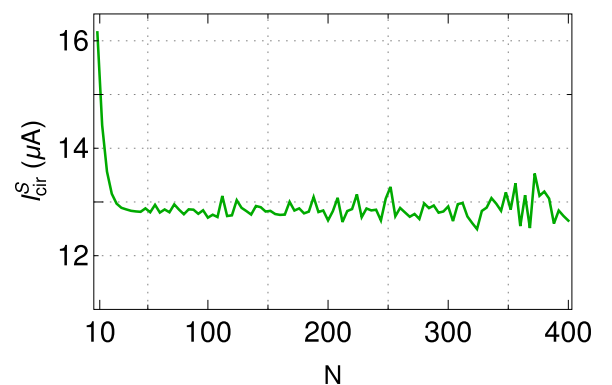


FIG. 11. Effect of ring size. Dependence of spin circular current as a function of ring size N . The results are worked out for the symmetric junction configuration setting the Fermi energy at 1.5 eV.

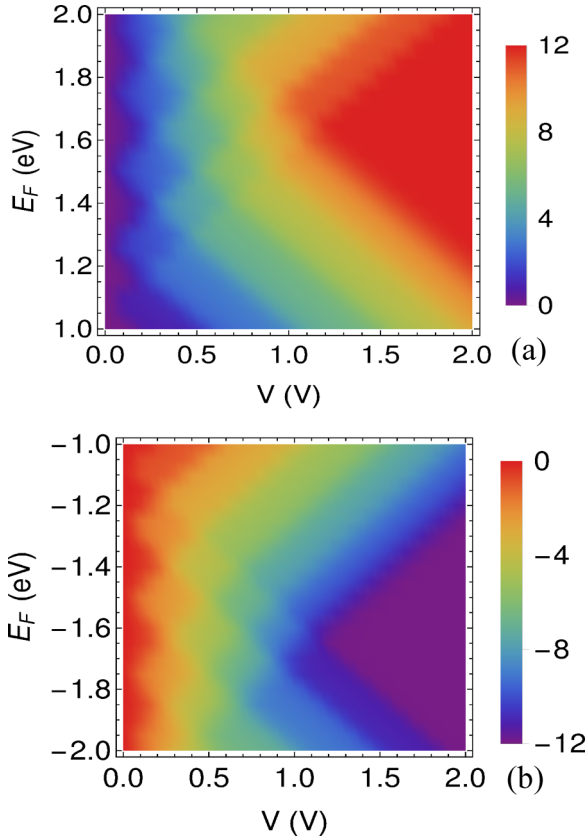


FIG. 12. Density plot. Simultaneous variation of spin circular current as functions of Fermi energy and the bias voltage. In (a), we vary E_F in positive energy side, while in (b), E_F is varied in the negative energy side. The results are worked out for a 32-site AFM ring considering symmetric ring-electrode junction configuration. The color bars denote the spin current in units of μA .

bias voltage and Fermi energy are varied in a wide range. In Fig. 12(a), the spin current is shown by varying E_F in the positive energy side, while for the negative energy side the current is given in Fig. 12(b). Quite interesting features are obtained. For a wide range of E_F , we can have the possibility to get a high circular spin current, and changing the Fermi energy we can selectively regulate the current. Moreover, the sign of the current can also be altered by adjusting the Fermi energy in the appropriate region. All these features depend on the contributing peaks and dips of the current density profile around the Fermi energy. From the results we can infer that to have the best possible response we need to make a thorough scan over the entire allowed energy window.

8. Is the full compensation of magnetization required?

At this stage, one obvious question may appear what is the necessity of full compensation for magnetization in the ring? More specifically, we can say how the circular spin current is sensitive if we slightly deviate from the condition of full elimination of net magnetization. To reveal this fact, in Fig. 13, we make a comparative analysis between two rings. In one ring we consider full compensation of magnetization like previous discussion. In the other ring we slightly deviate from the condition of full compensation, and in the lowest order, it is done just by flipping one magnetic moment

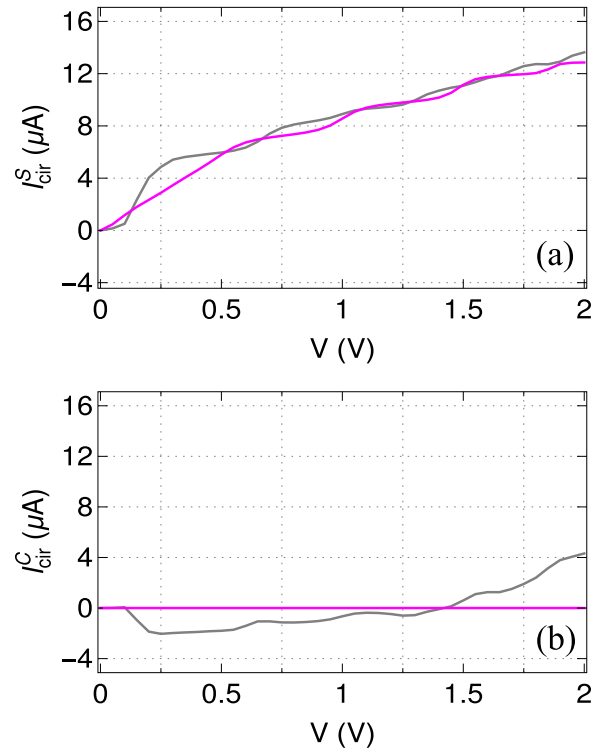


FIG. 13. Comparative analysis of (a) spin and (b) charge circular currents between the magnetic ring with full compensation of magnetization (magenta) and the ring without full compensation (gray). For the later ring, just one magnetic moment is flipped in the opposite direction (here the magnetic moment in site number 13 is considered). The results are computed for $E_F = 1.2$ eV considering the symmetric junction configuration in a 32-site ring.

from its initial orientation. For these two rings, the results are shown by the magenta and gray curves respectively. In Fig. 13, we present the results of both spin and charge circular currents as a function of bias voltage, those are computed for the symmetric junction configuration placing the Fermi energy at 1.2 eV. When the net magnetization is zero, the charge current becomes zero [magenta curve of Fig. 13(b)], as expected. However, a nonzero charge current is generated once the vanishing condition of net magnetization is deviated [gray curve of Fig. 13(b)]. The appearance of nonzero charge current is due to the breaking of the symmetry between the upper and lower arms of the ring. The notable thing is that, though finite charge current is obtained, it is too less compared to the spin circular current as clearly seen by comparing the results given in Figs. 13(a) and 13(b). Moreover, the spin currents in the two rings are also almost comparable to each other [magenta and gray curves of Fig. 13(a)]. From these results we can emphasize that, to have pure spin current, of course the full compensation of magnetization is needed. But a slight variation does not influence the behavior significantly, which again proves the robustness of our analysis.

B. Nanojunction with magnetic moments in upper arm of the ring along $+Z$ and lower arm along $-Z$

The characteristic features of bias-driven circular spin current discussed above in Sub-Sec. A are for the

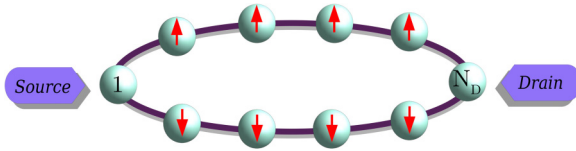


FIG. 14. Ring nanojunction, where the magnetic moments in the upper and lower arms are oriented along $+Z$ and $-Z$ directions, respectively.

antiferromagnetic ring with a specific arrangement of local magnetic moments where the neighboring moments are oriented along $\pm Z$ directions. That ring is referred to as ring-1. In the present section, we consider another arrangement of magnetic moments, keeping the condition of zero net magnetization. Such an arrangement is schematically shown in Fig. 14, where in one arm of the ring all the magnetic moments are oriented along $+Z$, and in the other arm the moments are oriented along $-Z$. We call this ring as ring-2. The aim of this section is to check whether ring-2 is capable of producing a circular spin current like the previous ring.

In Fig. 15, we present the variation of spin circular current as a function of bias voltage for the ring-2 system, at four distinct values of E_F , like what is done for the case of ring-1 system in Fig. 5. The ring size and the junction configuration remain unchanged to have a direct comparison between the results of rings 1 and 2. It is clearly seen that for ring-2 finite spin current is obtained and, most importantly, the magnitude of the current is much higher than the ring-1 case, for a particular Fermi energy. Achieving of higher spin current in ring 2 compared to the ring 1 is directly linked with the arrangement of local magnetic moments at different lattice sites. In ring 1, the neighboring magnetic moments are arranged in opposite directions, whereas for the case of ring 2, it seems that two ferromagnetic arms are coupled at the two end points. Because of the arrangements, in ring 1, much higher spin-dependent scattering takes place than the ring 2, resulting a lesser spin current in the former one. The other characteristic features remain almost same, as expected.

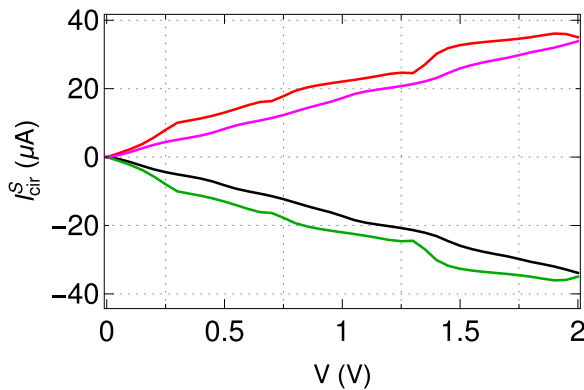


FIG. 15. Dependence of circular spin current with bias voltage at four distinct values of E_F for the ring-2 (similar to Fig. 5), where the black, green, red and purple curves are for $E_F = -2, -1, 1, 2$, respectively. The results are worked out for the symmetric ring-electrode junction setup, considering $N = 32$.

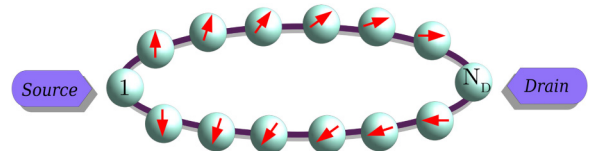


FIG. 16. Schematic view of an antiferromagnetic ring with a different texture of magnetic moments compared to what is taken into account in Fig. 1 and Fig. 14. Starting from a magnetic moment aligned along $+Z$ direction in the upper arm, each magnetic moment is rotated by a specific angle, and in the lower arm the opposite configuration is considered such that the net magnetization of the ring becomes zero. In the upper arm, θ_i is scaled from 0 to $\pi/2$, and accordingly, in the lower arm it is scaled from π to $3\pi/2$. For all these moments we set the azimuthal angle $\phi_i = 0$. The ring is coupled symmetrically to source and drain electrodes.

C. Ring nanojunction where the AFM ring contains textured magnetic moments

The results discussed so far are performed for the antiferromagnetic rings where the magnetic moments are aligned along $\pm Z$ directions. Under this condition, spin-dependent scattering matrix ($\vec{h}_i \cdot \vec{\sigma}$) becomes “diagonal,” and thus no spin-flipping takes place. It is indeed required to inspect how the spin-flip scattering affects the behavior of spin circular current. To reveal this fact, we consider a specific texture of magnetic moments in the ring, as shown in Fig. 16, and we refer to this ring as ring 3. The moments in the two arms are arranged in such a way that they are opposite to each other, resulting in a vanishing net magnetization in the ring. As the orientations of magnetic moments are different compared to $\pm Z$ directions, both σ_x and σ_y are involved, and hence the spin-dependent scattering matrix contains off-diagonal elements. Because of this, we get spin-flip scattering while traversing the electrons through the ring nanojunction. For the AFM ring with such a textured magnetic moments, the dependence of spin circular current with bias voltage is given in Fig. 17. Four different curves are shown, associated with four distinct Fermi energies, to have a direct comparison with the results presented in Fig. 15. The results are com-

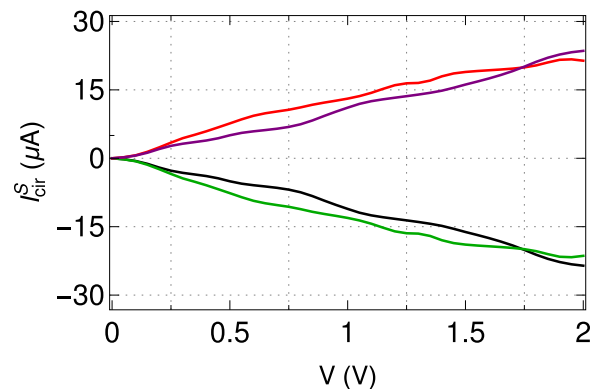


FIG. 17. Spin circular current vs bias voltage for ring 3 where the magnetic moments are arranged as shown in Fig. 16. All the required physical parameters are same as used in Fig. 15, to have a direct comparison of the results.

puted for the identical ring size and for the same junction configuration (symmetric ring-electrode junction). Since the upper and lower arms are identical in length and the magnetic configurations are opposite to each other, charge circular current does not appear. Thus we get pure spin circular current. Comparing the results with Fig. 15 it is found that the overall degree of spin current decreases. This reduction is solely due to the spin-dependent scattering at different magnetic sites. More spin-flip scattering means, more mixing of up and down spins, resulting a decrement of pure spin current. Though the current gets reduced, it is still reasonably large which is quite interesting. Thus it can be manifested that bias-driven pure spin circular current can be obtained in noncollinear antiferromagnetic systems as well.

IV. EXPERIMENTAL POSSIBILITIES FOR DESIGNING AFM RINGS

Nowadays different kinds of efficient and sophisticated techniques are available through which patterned magnetic rings can safely be designed. The most common methodologies are nanoscale lithography [63], electron beam lithography [64], and silicon etching processes [65]. The droplet epitaxy method [66] is also used quite frequently to design magnetic ring geometries. Sometimes wet mixing prescription is also employed for synthesizing antiferromagnetic rings [67]. Probably, the most controlled and patterned geometries can be constructed by dewetting magnetic nanoparticle solution in a substrate. Yang and co-workers have made significant contributions along this line. The capillary force lithography followed by reactive etching method can also be considered

for designing magnetic nanorings with good accuracy [68]. With these plenty of experimental possibilities, we may think that the antiferromagnetic nanorings proposed in our work can be substantiated in suitable laboratories.

V. CLOSING REMARKS

Appearance of pure spin current in an “isolated” nanoring (not connected to electronic baths) is a well known fact and can be generated in different ways, but in an open quantum system it is a new phenomenon, and especially in a magnetic system with zero net magnetization. In this work, we report this phenomenon for the first time, to the best of our concern, considering an antiferromagnetic ring nanojunction. Illustrating the quantum system within a TB framework, all the results are worked out based on the standard Green’s function formalism. The bias-driven circular current is obtained by evaluating the individual bond currents with the help of a correlated Green’s function. The effects of ring-electrode interface configuration, impurities, spin-dependent scattering parameter, ring size, Fermi energy, ring-electrode coupling strength and arrangements of magnetic moments on spin circular current are critically investigated. For some specific input conditions, a charge circular current may appear but its magnitude becomes too small compared to the spin counterpart. All the results of spin circular current are valid for a broad range of physical parameters which proves the robustness of our work. Our analysis may provide a new route of generating and manipulating bias-driven pure spin circular current in different kinds of magnetic materials with vanishing net magnetization.

-
- [1] M. Büttiker, Y. Imry, and R. Landauer, Josephson behavior in small normal one-dimensional rings, *Phys. Lett. A* **96**, 365 (1983).
 - [2] R. A. Smith, and V. Ambegaokar, Systematic calculation of moment of flux-dependent currents in single mesoscopic rings, *Europhys. Lett.* **20**, 161 (1992).
 - [3] E. Gambetti-Cèsare, D. Weinmann, R. A. Jalabert, and P. Brune, Disorder-induced enhancement of the persistent current for strongly interacting electrons in one-dimensional rings, *Europhys. Lett.* **60**, 120 (2002).
 - [4] H. F. Cheung, Y. Gefen, E. K. Riedel, and W. H. Shih, Persistent currents in small one-dimensional metal rings, *Phys. Rev. B* **37**, 6050 (1988).
 - [5] Y. Gefen, Y. Imry, and M. Ya. Azbel, Quantum oscillations and the Aharonov-Bohm effect for parallel resistors, *Phys. Rev. Lett.* **52**, 129 (1984).
 - [6] J. Yi, J. H. Wei, J. Hong, and S.-Ik Lee, Giant persistent currents in the open Aharonov-Bohm rings, *Phys. Rev. B* **65**, 033305 (2001).
 - [7] W. Hofstetter, J. König, and H. Schoeller, Kondo correlations and the Fano effect in closed Aharonov-Bohm interferometers, *Phys. Rev. Lett.* **87**, 156803 (2001).
 - [8] H. F. Cheung and E. K. Riedel, Persistent currents in mesoscopic rings and cylinders, *Phys. Rev. Lett.* **62**, 587 (1989).
 - [9] P. A. Orellana and M. Pacheco, Persistent current magnification in a double quantum-ring system, *Phys. Rev. B* **71**, 235330 (2005).
 - [10] S. K. Maiti, J. Chowdhury, and S. N. Karmakar, Enhancement of persistent current in mesoscopic rings and cylinders: shortest and next possible shortest higher-order hopping, *J. Phys.: Condens. Matter* **18**, 5349 (2006).
 - [11] L. P. Levy, G. Dolan, J. Dunsmuir, and H. Bouchiat, Magnetization of mesoscopic copper rings: Evidence for persistent currents, *Phys. Rev. Lett.* **64**, 2074 (1990).
 - [12] E. M. Q. Jariwala, P. Mohanty, M. B. Ketchen, and R. A. Webb, Diamagnetic persistent current in diffusive normal-metal rings, *Phys. Rev. Lett.* **86**, 1594 (2001).
 - [13] V. Chandrasekhar, R. A. Webb, M. J. Brady, M. B. Ketchen, W. J. Gallagher, and A. Kleinsasser, Magnetic response of a single, isolated gold loop, *Phys. Rev. Lett.* **67**, 3578 (1991).
 - [14] H. Bluhm, N. C. Koshnick, J. A. Bert, M. E. Huber, and K. A. Moler, Persistent currents in normal metal rings, *Phys. Rev. Lett.* **102**, 136802 (2009).
 - [15] J. Splettstoesser, M. Governale, and U. Zülicke, Persistent current in ballistic mesoscopic rings with Rashba spin-orbit coupling, *Phys. Rev. B* **68**, 165341 (2003).

- [16] Q.-F. Sun, X. C. Xie, and J. Wang, Persistent spin current in a mesoscopic hybrid ring with spin-orbit coupling, *Phys. Rev. Lett.* **98**, 196801 (2007).
- [17] Q.-F. Sun, X. C. Xie, and J. Wang, Persistent spin current in nanodevices and definition of the spin current, *Phys. Rev. B* **77**, 035327 (2008).
- [18] A. A. Shokri and M. Mardaani, Spin-flip effect on electrical transport in magnetic quantum wire systems, *Solid State Commun.* **137**, 53 (2006).
- [19] M. Mardaani and A. A. Shokri, Electrical conductance in a typical linear and cyclic quantum wire, *Int. J. Nanotechnol.* **6**, 1050 (2009).
- [20] M. Dey, S. K. Maiti, and S. N. Karmakar, Topological effect on spin transport in a magnetic quantum wire: Green's function approach, *J. Comput. Theor. Nanosci.* **8**, 253 (2011).
- [21] L. Benini, A. Mukherjee, A. Chakrabarti, and R. A. Römer, Spin-polarized localization in a magnetized chain, *Sci. Rep.* **9**, 5930 (2019).
- [22] M. Patra and S. K. Maiti, Bias-induced circular spin current: Effects of environmental dephasing and disorder, *Phys. Rev. B* **100**, 165408 (2019).
- [23] Y. A. Bychkov and E. I. Rashba, Oscillatory effects and the magnetic susceptibility of carriers in inversion layers, *J. Phys. C: Solid State Phys.* **17**, 6039 (1984).
- [24] G. Dresselhaus, Spin-orbit coupling effects in zinc blende structures, *Phys. Rev.* **100**, 580 (1955).
- [25] S. Premasiri, S. K. Radha, S. Sucharitakul, U. R. Kumar, R. Sankar, F.-C. Chou, Y.-T. Chen, and X. P. A. Gao, Tuning rashba spin-orbit coupling in gated multilayer inse, *Nano Lett.* **18**, 4403 (2018).
- [26] Y.-H. Su, S.-H. Chen, C. D. Hu, and C.-R. Chang, Competition between spin-orbit interaction and exchange coupling within a honeycomb lattice ribbon, *J. Phys. D: Appl. Phys.* **49**, 015305 (2016).
- [27] K. Tagami and M. Tsukada, Current-controlled magnetism in T-shape tape-porphyrin molecular bridges, *Curr. Appl. Phys.* **3**, 439 (2003).
- [28] G. Stefanucci, E. Perfetto, S. Bellucci, and M. Cini, Generalized waveguide approach to tight-binding wires: Understanding large vortex currents in quantum rings, *Phys. Rev. B* **79**, 073406 (2009).
- [29] D. Rai, O. Hod, and A. Nitzan, Circular currents in molecular wires, *J. Phys. Chem. C* **114**, 20583 (2010).
- [30] S. Nakanishi and M. Tsukada, The theory of microscopic current distribution in molecular bridge structures, *Surf. Sci.* **438**, 305 (1999).
- [31] L. Wang, K. Tagami, and M. Tsukada, Quantum transport through multiterminal phenalenyl molecular bridges, *Jpn. J. Appl. Phys.* **43**, 2779 (2004).
- [32] M. Tsukada, K. Tagami, K. Hirose, and N. Kobayashi, Theory of quantum conductance of atomic and molecular bridges, *J. Phys. Soc. Jpn.* **74**, 1079 (2005).
- [33] D. Rai, O. Hod, and A. Nitzan, Magnetic fields effects on the electronic conduction properties of molecular ring structures, *Phys. Rev. B* **85**, 155440 (2012).
- [34] V. Baltz, A. Manchon, M. Tsoi, T. Moriyama, T. Ono, and Y. Tserkovnyak, Antiferromagnetic spintronics, *Rev. Mod. Phys.* **90**, 015005 (2018).
- [35] T. Jungwirth, J. Sinova, X. Matri, J. Wunderlich, and C. Felser, The multiple directions of antiferromagnetic spintronics, *Nat. Phys.* **14**, 200 (2018).
- [36] M. B. Jungfleisch, W. Zhang, and A. Hoffmann, Perspectives of antiferromagnetic spintronics, *Phys. Lett. A* **382**, 865 (2018).
- [37] P. Wadley, B. Howells, J. Zelezný, C. Andrews, V. Hills, R. P. Campion, V. Novák, K. Olejník, F. Maccherozzi, S. S. Dhesi, S. Y. Martin, T. Wagner, J. Wunderlich, F. Freimuth, Y. Mokrousov, J. Kunes, J. S. Chauhan, M. J. Grzybowski, A. W. Rushforth, K. W. Edmonds, B. L. Gallagher, and T. Jungwirth, Electrical switching of an antiferromagnet, *Science* **351**, 587 (2016).
- [38] T. Kosub, M. Kopte, and R. Hühne, Purely antiferromagnetic magnetoelectric random access memory, *Nat. Commun.* **8**, 13985 (2017).
- [39] P. Němec, M. Fiebig, T. Kampfrath, and A. V. Kimel, Antiferromagnetic opto-spintronics, *Nat. Phys.* **14**, 229 (2018).
- [40] S. Middey, S. Debnath, P. Mahadevan, and D. D. Sarma, NaOsO₃: A high Neel temperature *5d* oxide, *Phys. Rev. B* **89**, 134416 (2014).
- [41] J.-J. Liao, Y.-Z. Nie, X. Wang, Q. Xia, R. Xiong, and G. Guo, Prediction of antiferromagnetic metal-rich chalcogenide monolayers M₂X (M = Ti, Zr, Hf and X = S, Se, Te) with high Néel temperature, *Appl. Surf. Sci.* **586**, 152821 (2022).
- [42] J. Železný, H. Gao, K. Výborný, J. Zemen, J. Mašek, Aurélien Manchon, J. Wunderlich, Jairo Sinova, and T. Jungwirth, Relativistic néel-order fields induced by electrical current in antiferromagnets, *Phys. Rev. Lett.* **113**, 157201 (2014).
- [43] D. S. Fisher and P. A. Lee, Relation between conductivity and transmission matrix, *Phys. Rev. B* **23**, 6851 (1981).
- [44] S. Datta, *Electronic Transport in Mesoscopic Systems* (Cambridge University Press, Cambridge, 1997).
- [45] S. Datta, *Quantum Transport: Atom to Transistor* (Cambridge University Press, Cambridge, 2005).
- [46] M. D. Ventra, *Electrical Transport in Nanoscale Systems* (Cambridge University Press, Cambridge, 2008).
- [47] S. Datta, *Lessons from Nanoelectronics* (World Scientific, 2012).
- [48] H. Jiang, L. Wang, Q.-F. Sun, and X. C. Xie, Numerical study of the topological Anderson insulator in HgTe/CdTe quantum wells, *Phys. Rev. B* **80**, 165316 (2009).
- [49] X. T. An, Y. Y. Zhang, J. J. Liu, S. S. Li, Quantum spin Hall effect induced by electric field in silicene, *Appl. Phys. Lett.* **102**, 043113 (2013).
- [50] Q. Zhang, Z. Lin, and K. S. Chan, Spin polarization switching in monolayer graphene through a Rashba multi-barrier structure, *Appl. Phys. Lett.* **102**, 142407 (2013).
- [51] S. Abdelouahed, A. Ernst, and J. Henk, Spin-split electronic states in graphene: Effects due to lattice deformation, Rashba effect, and adatoms by first principles, *Phys. Rev. B* **82**, 125424 (2010).
- [52] Z. F. Zhang, Z. G. Zhu, and G. Su, Theory of nonlinear response for charge and spin currents, *Phys. Rev. B* **104**, 115140 (2021).
- [53] S. Souma and B. K. Nikolić, Spin hall current driven by quantum interferences in mesoscopic rashba rings, *Phys. Rev. Lett.* **94**, 106602 (2005).
- [54] S. Souma and B. K. Nikolić, Modulating unpolarized current in quantum spintronics: Visibility of spin-interference effects in

- multichannel Aharonov-Casher mesoscopic rings, *Phys. Rev. B* **70**, 195346 (2004).
- [55] S. J. Xiong and Y. Xiong, Anderson localization of electron states in graphene in different types of disorder, *Phys. Rev. B* **76**, 214204 (2007).
- [56] S. Aigner, L. D. Pietra, Y. Japha, O. Entin-Wohlman, T. David, R. Salem, R. Folman, and J. Schmiedmayer, Long-range order in electronic transport through disordered metal films, *Science* **319**, 1226 (2008).
- [57] P. W. Anderson, Absence of diffusion in certain random lattices, *Phys. Rev.* **109**, 1492 (1958).
- [58] P. A. Lee and T. V. Ramakrishnan, Disordered electronic systems, *Rev. Mod. Phys.* **57**, 287 (1985).
- [59] N. F. Mott and W. D. Twose, The theory of impurity conduction, *Adv. Phys.* **10**, 107 (1961).
- [60] K. Walczak, The role of quantum interference in determining transport properties of molecular bridges, *Cent. Eur. J. Chem.* **2**, 524 (2004).
- [61] K. Walczak, Current fluctuations of polymeric chains, *Physica Status Solidi (b)* **241**, 2555 (2004).
- [62] K. Walczak, Charging effects in biased molecular devices, *Physica E* **25**, 530 (2005).
- [63] M. Winzer, M. Kleiber, N. Dix, and R. Wiesendanger, Fabrication of nano-dot-and nano-ring-arrays by nanosphere lithography, *Appl. Phys. A* **63**, 617 (1996).
- [64] S. M. Weekes, F. Y. Ogrin, and W. A. Murray, Fabrication of large-area ferromagnetic arrays using etched nanosphere lithography, *Langmuir* **20**, 11208 (2004).
- [65] Z. Cui, J. Rothman, M. Klaui, L. Lopez-Diaz, C. A. F. Vaz, and J. A. C. Bland, Fabrication of magnetic rings for high density memory devices, *Microelectron. Eng.* **61-62**, 577 (2002).
- [66] C. Z. Tong, and S. F. Yoon, Nanotechnology Investigation of the fabrication mechanism of self-assembled GaAs quantum rings grown by droplet epitaxy, *Nanotechnology* **19**, 365604 (2008).
- [67] A. V. Kurilova, A. E. Sokolov, A. L. Sukhachev, O. S. Ivanova, K. V. Bogdanov, M. A. Baranov and A. Yu. Dubavik, Synthesizing antiferromagnetic $\alpha - \text{Fe}_2\text{O}_3 - \text{rGO}$ discs: Their magnetic and magneto-optical properties, *Bull. Russ. Acad. Sci. Phys.* **86**, 610 (2022).
- [68] S. Y. Lee, J.-R. Jeong, S.-H. Kim, S. Kim, and S.-M. Yang, Arrays of ferromagnetic nanorings with variable thickness fabricated by capillary force lithography, *Langmuir* **25**, 12535 (2009).